remote sensing

MDPI

Article

Mud Volcanism at the Taman Peninsula: Multiscale Analysis of Remote Sensing and Morphometric Data

Tatyana N. Skrypitsyna [1], Igor V. Florinsky [2,*], Denis E. Beloborodov [3] and Olga V. Gaydalenok [4]

[1] Department of Photogrammetry, Moscow State University of Geodesy and Cartography (MIIGAiK), 4 Gorokhovsky Lane, 105064 Moscow, Russia; tatyana.skrypitsyna@yandex.ru
[2] Institute of Mathematical Problems of Biology, Keldysh Institute of Applied Mathematics, Russian Academy of Sciences, 1 Prof. Vitkevich St., 142290 Pushchino, Moscow Region, Russia
[3] Laboratory of Earthquake Physics and Rock Instability, Schmidt Institute of Physics of the Earth, Russian Academy of Sciences, 10-1 B. Gruzinskaya St., 123242 Moscow, Russia; beloborodov@ifz.ru
[4] Laboratory of Neotectonics and Recent Geodynamics, Geological Institute, Russian Academy of Sciences, 7-1, Pyzhevsky Lane, 119017 Moscow, Russia; ogaydalen@yandex.ru
* Correspondence: iflor@mail.ru

Received: 9 October 2020; Accepted: 13 November 2020; Published: 16 November 2020

Abstract: Mud volcanism is observed in many tectonically active regions worldwide. One of the typical areas of mud volcanic activity is the Taman Peninsula, Russia. In this article, we examine the possibilities of multiscale analysis of remote sensing and morphometric data of different origins, years, scales, and resolutions for studying mud volcanic landscapes. The research is exemplified by the central-northern margin of the Taman Peninsula, where mud volcanism has only been little studied. The data set included one arc-second gridded Advanced Land Observing Satellite World three-dimensional (3D) digital surface model (AW3D30 DSM); a Corona historical declassified satellite photography; high-resolution imagery from an unmanned aerial survey (UAS) conducted with a multi-copter drone DJI Phantom 4 Pro, as well as a series of 1-m gridded morphometric models, including 12 curvatures (minimal, maximal, mean, Gaussian, unsphericity, horizontal, vertical, difference, vertical excess, horizontal excess, accumulation, and ring one) derived from UAS-based images. The data analysis allowed us to clarify the conditions of neotectonic development in the central-northern margin of the Taman Peninsula, as well as to specify manifestations of the mud volcanism in this region. In particular, we were able to detect minor and weakly topographically expressed mud volcanic features (probably, inactive gryphons, and salses), which are hidden by long-term farming practice (e.g., ploughed and covered by soil).

Keywords: unmanned aerial survey; digital elevation model; geomorphometry; mud volcano

1. Introduction

Mud volcanism, which is usually associated with the processes of deep degassing and migration of fluids, is observed in many tectonically active regions worldwide [1–3]. One of the typical areas of mud volcanic activity is the Taman Peninsula located between the Black Sea, the Sea of Azov, and the Kerch Strait (Figure 1a) in the south-western Russia [4,5].

In this region, large and active mud volcanoes are well known (Figure 1a) and systematically studied [6–8]. At the same time, minor, inactive, and weakly topographically expressed mud volcanic structures are poorly mapped and understood. This is because most of such features are located in arable lands, pastures, and vineyards, wherein they can be leveled and/or partly hidden, due to long-term farming practice. However, knowledge on these minor structures is important for a better understanding of the dynamics and evolution of the mud volcanism and related processes.

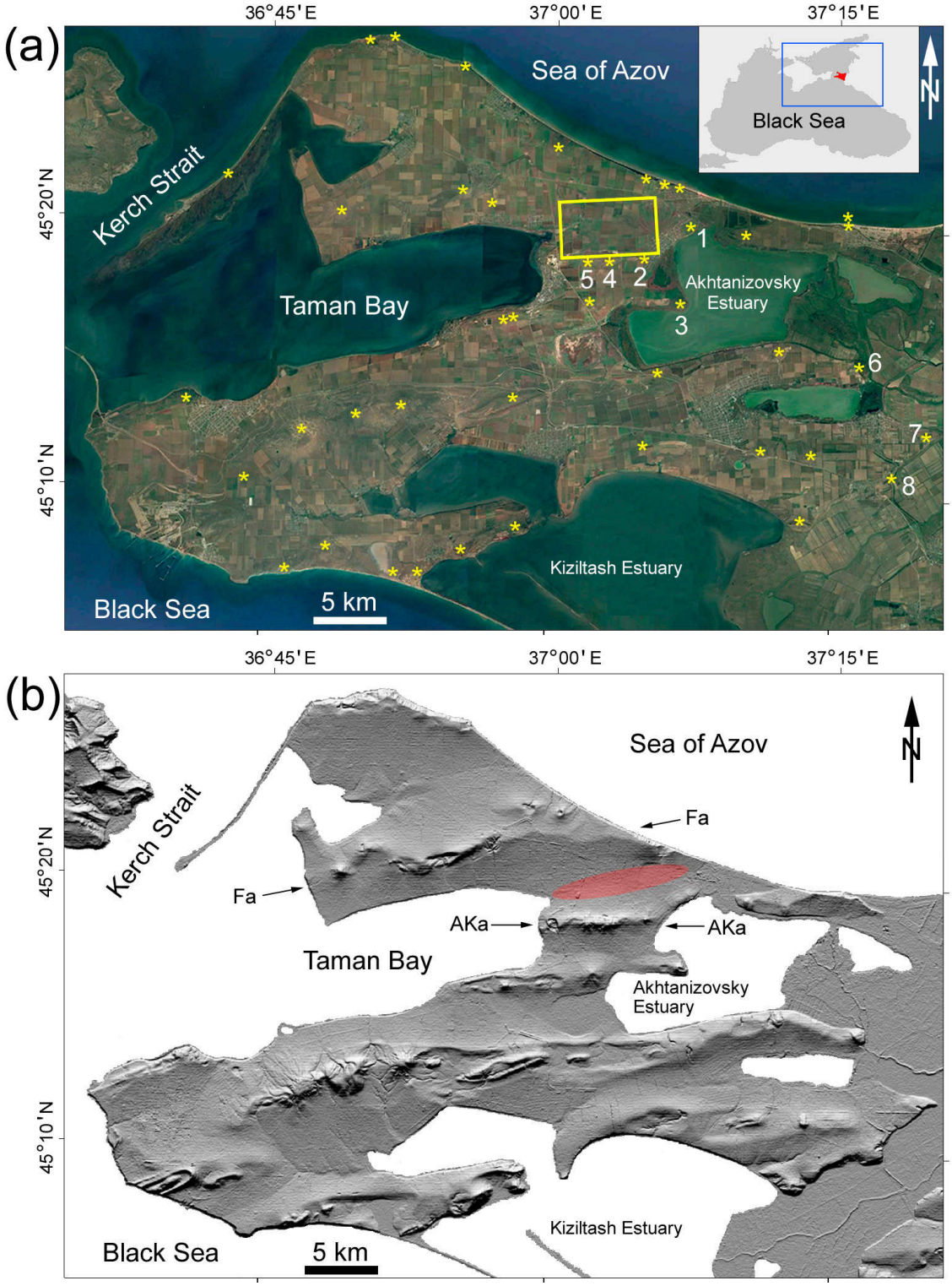

Figure 1. The Taman Peninsula: (**a**) Distribution of large and active mud volcanoes (yellow asterisks; for their coordinates, see [8]), and the geographical position of the study area on the background of the Google Earth image mosaic (yellow frame, see Sections 2 and 3.2). Mud volcanoes discussed in the text: 1—Severo-Akhtanizovsky and its gryphon field, 2—Akhtanizovskaya Sopka, 3—Boris-and-Gleb, 4—East and 5—West Tsymbals, 6—Dubovy Rynok, 7—Strelchanskaya, 8—Bely Khutor. The insert map: the red area indicates the position of the Taman Peninsula; the blue frame shows the location of the tectonic frame of the Kerch-Taman folded zone (see Figure 2). (**b**) The AW3D30-based hill-shaded map (Sun azimuth 315° and altitude 45°). The pink oval is the syncline between the Fontalovskaya (Fa) and Anastasievskaya–Krasnodar (AKa) anticlines discussed in the text.

Detecting and studying hidden geological features of various origins are commonly facilitated by using remote sensing data [9–11], digital terrain models, and geomorphometric analysis [12]. For these purposes, one can utilize information of various types (satellite and aerial imagery taken in different ranges of the spectrum), scales (from continental to local), and resolutions (from meters to tens and hundreds of meters). Recently, unmanned aerial systems (UASs), which are used in various scientific and industrial fields (see reviews [13–22]), have become a tool for monitoring active mud volcanoes [23–25]. However, as far as we know, neither traditional remote sensing approaches nor UAS-based ones have been used for detecting hidden mud volcanic features.

In this article, we examine the possibilities of multiscale analysis of remote sensing and morphometric data of different origins, years, scales, and resolutions for studying landscapes with hidden mud volcanic features. The study is exemplified by the central-northern margin of the Taman Peninsula, where mud volcanism has only been little studied.

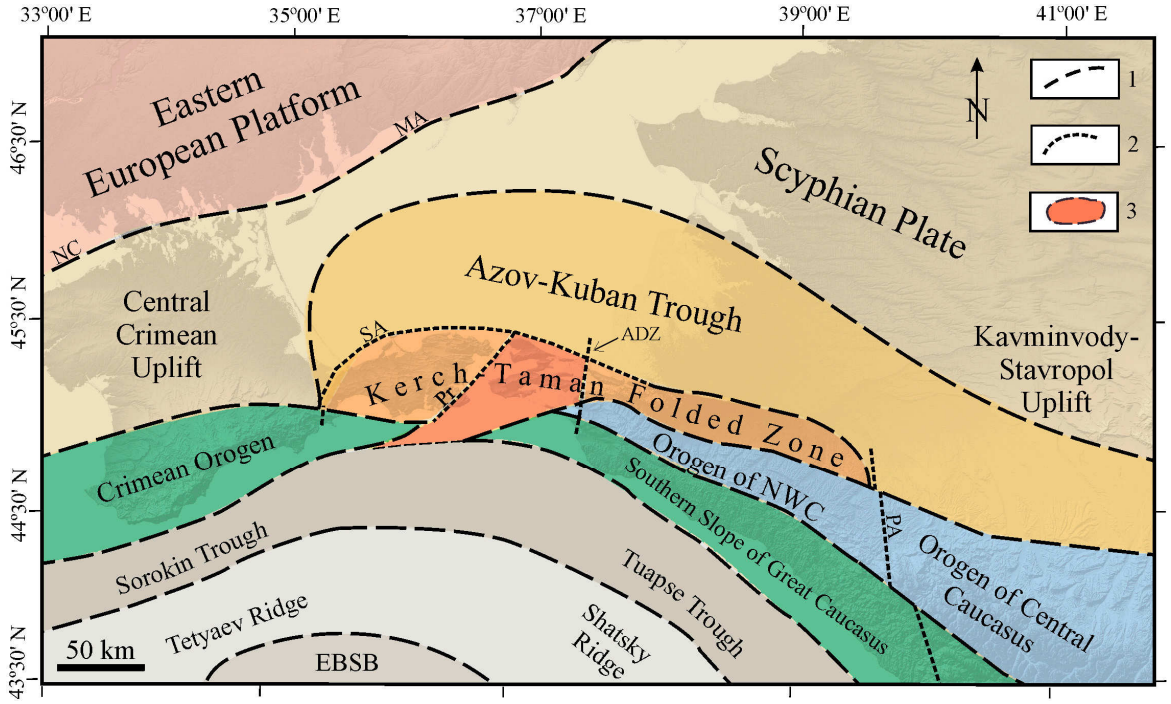

Figure 2. Tectonic frame of the Kerch-Taman folded zone. 1—boundaries of tectonic structures, 2—fault zones, 3—the Kerch-Taman transverse (periclinal) trough. NWC—North-Western Caucasus, EBSB—Eastern Black Sea Basin. Fault zones: ADZ—Anapa–Dzhiginka, MA—Main Azov, NC—North Crimean, PA—Pshekh–Adler, Pr—Pravdinsky, SA—Southern Azov. For the location, see Figure 1a, the inset map, the blue frame.

2. Study Area

Geomorphically, the Taman Peninsula is an alluvial plain terrain with systems of north-east- and almost west-east-striking narrow, low ridges that are divided by wide valleys and depressions, including estuaries [26] (Figure 1b). Elevations range from 0 m to 142 m above sea level. Tectonically, the Taman Peninsula corresponds to the Kerch–Taman transverse (periclinal) trough of the Kerch–Taman folded zone located between the Crimean Orogen and the Central Crimean Uplift in the west, the Kavminvody–Stavropol Uplift in the east, a non-deformed part of the Azov–Kuban Trough in the north, the orogen of North-Western Caucasus in the south-east, and structures of the Black Sea Basin in the south (Figure 2) [27]. The Kerch–Taman transverse trough is filled with the Oligocene–Lower Miocene Maikop Series marine deposits consisting of sandy-clayey rocks up to 3000 m thick [26]. In a broader tectonic context, the Kerch–Taman folded zone is a part of the Alpine–Himalayan folded

belt [28]. Generally, the regional tectonics is directly reflected in the topography: narrow ridges correspond to anticlines, while interridge valleys relate to synclines.

The territory belongs to the eastern part of the Kerch–Taman mud volcanic province. Large, recently active mud volcanoes are located along the anticline axes (Figure 1). Plastic clays of the Maikop Series are the source for the regional mud volcanism [4–7].

The study area is situated in the central-northern margin of the Taman Peninsula, between the Sea of Azov, the Taman Bay, and the Akhtanizovsky Estuary (Figure 1a). It is a part of a syncline covered by alluvial and deluvial upper Neogene loess loams [26]. In general, the terrain is relatively flat with elevations range from 12 m to 48 m above sea level. The syncline is located between the Fontalovskaya and Anastasievskaya–Krasnodar anticlines. There are several large, active mud volcanoes along both anticlines (Figure 1).

Geological study of the area is complicated due to the leveled topography, the lack of rock outcrops, and land-use practices, such as arable farming, pasturage, and viticulture (Figure 3). Slopes of large, active mud volcanic structures and gryphon fields are only partially plowed up (Figure 4a,b). However, minor, inactive mud volcanic features are completely plowed up and difficult identify (Figure 4c,d).

Figure 3. A typical landscape of the study area. One can see a field to the left, and a vineyard to the right (UAS-based image; for the unmanned aerial survey, see Section 3.3.1).

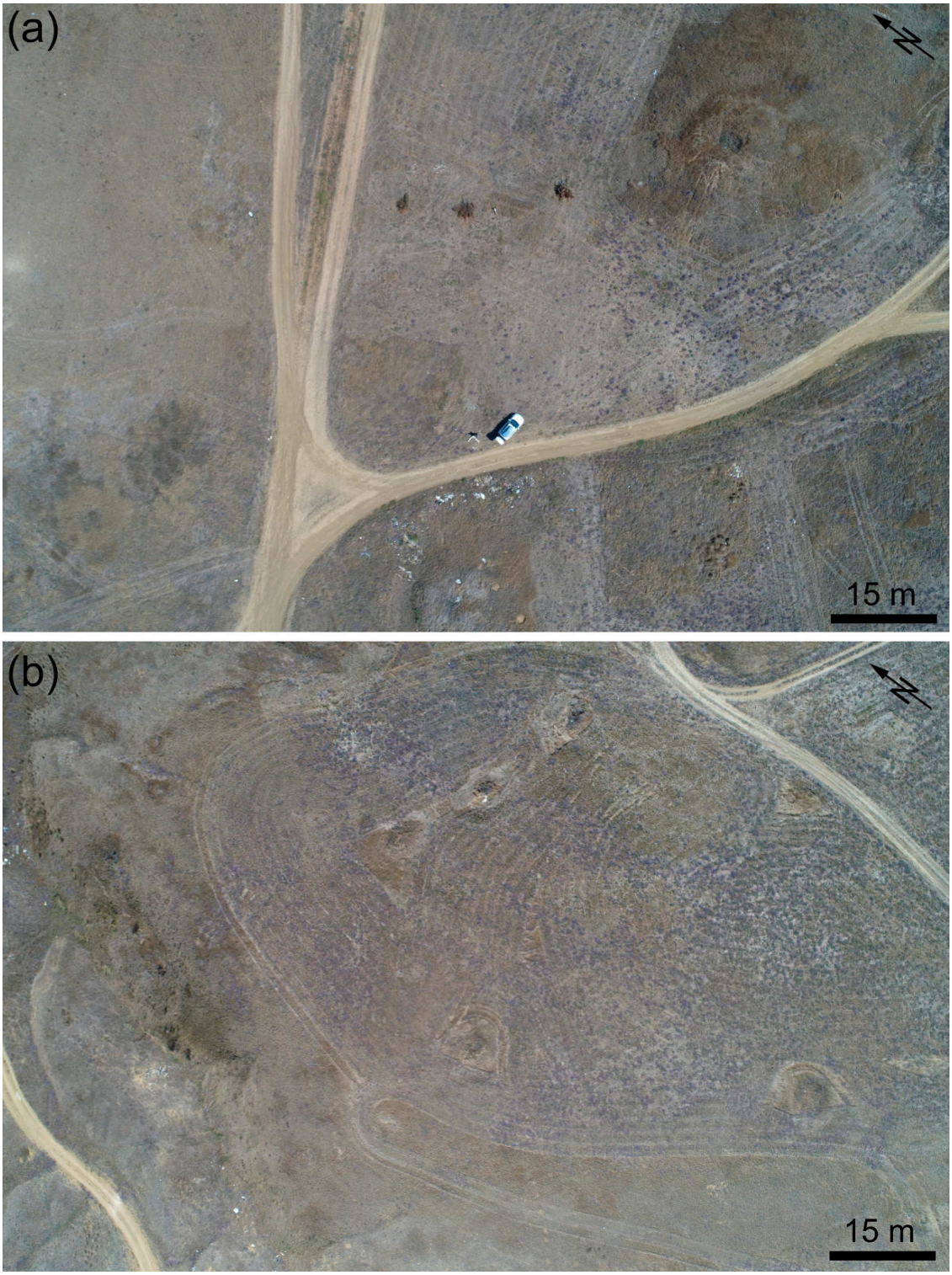

Figure 4. *Cont.*

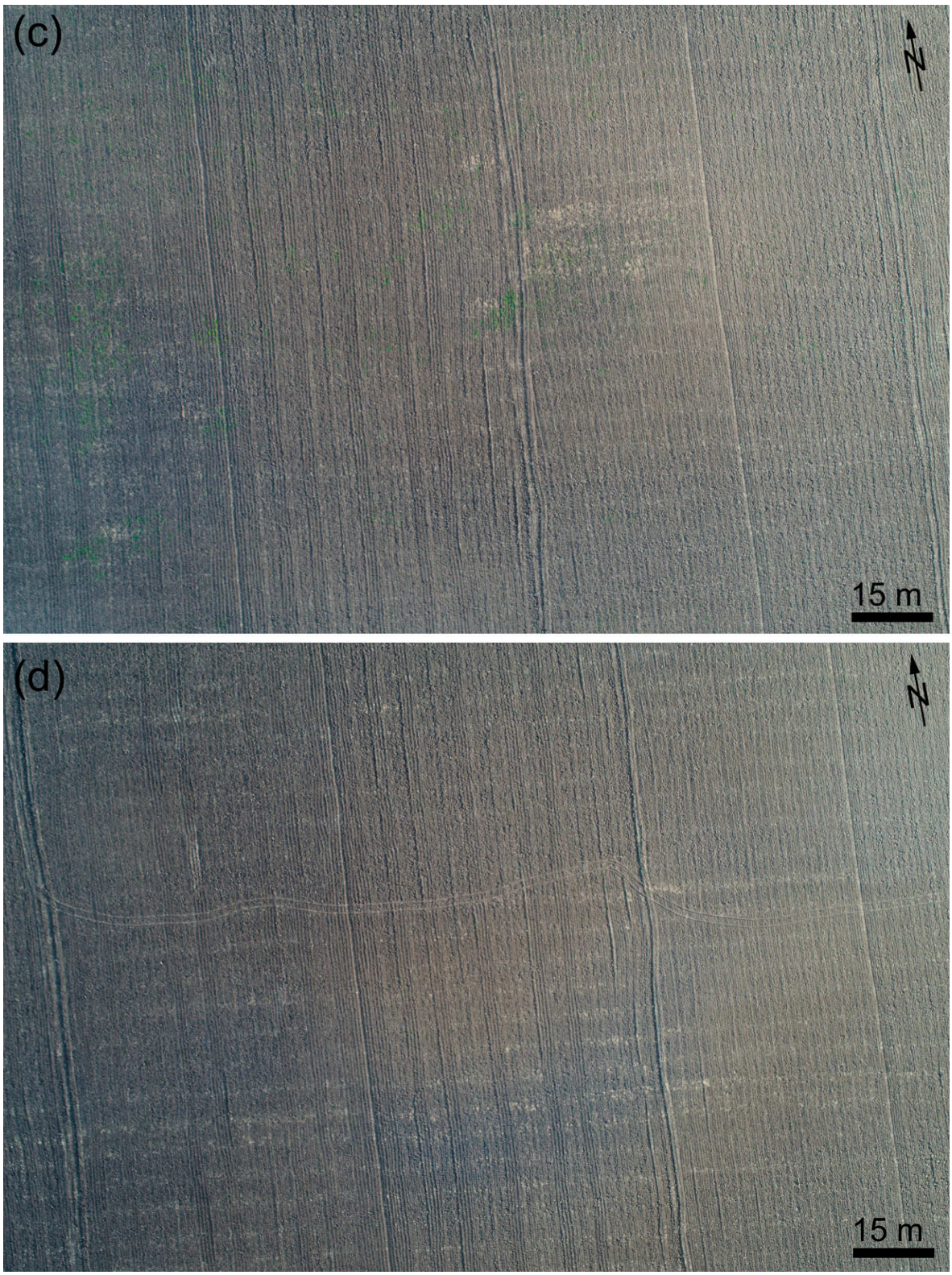

Figure 4. Examples of partial and complete plowing of mud volcanic structures (UAS-based imagery, see Section 3.3.1): (**a**) The Severo-Akhtanizovsky mud volcano (the upper right corner). (**b**) An active gryphon field nearby the Severo-Akhtanizovsky mud volcano. One can see arable furrows (preparation for planting a vineyard) around the mud volcano and gryphons. However, they themselves are not affected by plowing and are clearly visible. For their location, see Figure 1a. (**c**,**d**) Areas with two ring microstructures revealed by geomorphometric analysis (see Section 4). The structures are completely plowed up and cannot visually be identified. One can see arable furrows and field roads only. For the image and structure locations, see Section 3.3.

3. Materials and Methods

A general scheme for the study included an analysis of remote sensing data at three levels of scale and resolution. The first, regional level (a resolution of about 30 m) was intended to analyze a general position of the study area in the tectonic structure of the region. The second, subregional level (a resolution of about 3 m) was intended to detect lineaments associated with the geological evolution of the study area, as well as the primary identification of (partly) hidden microfeatures of mud volcanism. The third, local level (a resolution of 1 m) was intended to clarify the landscape position and geometry of some mud volcanic microstructures within a selected study site.

3.1. Regional Level

At the regional level, we used the Advanced Land Observing Satellite World 3D (AW3D30), a nearly-global one arc-second gridded digital surface model (DSM). AW3D30 DSM was photogrammetrically derived from 2.5-m resolution, visible-band stereo images that were acquired from the Advanced Land Observing Satellite (ALOS) in 2006–2011 [29]. AW3D30 DSM has the highest quality among free, nearly-global digital elevation models (DEMs) [30–32].

For the Taman Peninsula, we extracted a portion from the AW3D30 DSM v. 2.1 [33]. Next, we applied one of the most popular geomorphometric approaches: reflectance mapping or hill shading [34]. This approach has long been effectively used in geological studies for revealing and visualization of topographically manifested regional tectonic features [35,36]. A hill-shaded map with a resolution of 26 m (Figure 1b) was derived from the AW3D30 DSM using QGIS software.

3.2. Subregional Level

At the subregional level, we used a historical, declassified satellite photography of the study area (Figure 5a). This was a panoramic, visible-band monochromic image with a resolution of 2.7 m that was taken on 9 September 1969, by the camera J-1 onboard the KH-4A spacecraft, the Corona mission 1052 [37]. We utilized the Corona image DS1052-2122DF028_b.

We decided to use the Corona image for the following reason. Since the early 1970s, the study area has been intensively agriculturally developed: it has been ploughed up; orchards and vineyards have been created (Figure 3). Thus, at the subregional level, it is reasonable to use space or aerial photographs that were captured before the 1970s to simplify image interpretation.

Registration of the Corona image was performed by affine transformations [38] using MapInfo Pro 16.0 software. For the registration, we utilized binding points (i.e., road intersections) confidently identified on both the Corona image and two orthomosaics: (1) a UAS-based orthomosaic (a pixel size of 0.2 m) obtained in this study (see Section 3.3.2) and (2) a SPOT-6 orthomosaic (a pixel size of 1.8 m) generated in 2017.

We had to use two orthomosaics, because the coverage of the Corona image is about 75 km by 18 km. The UAS-based orthomosaic covers just a small portion of the Corona image: 3.25 km by 2.2 km. Thus, using the UAS-based orthomosaic allowed us to identify five binding points. Such a number of binding points is obviously insufficient for the registration of the Corona image. To fill this gap, we used the SPOT-6 orthomosaic. However, the time between capturing the Corona and SPOT images was almost 50 years, and the landscape has changed due to agricultural development. Thus, using the SPOT-6 orthomosaic allowed us to identify only 17 additional points. As a result, an average accuracy of the Corona image registration was about 20 m within the study area.

There are several causes for such a rough accuracy: (a) perspective distortions of the Corona image; (b) elevation ranging from 12 m to 48 m within the study area; and (c) uneven distribution of the 23 binding points. To increase the registration accuracy, one may perform a photogrammetric processing of a Corona image, including determination of its interior and exterior orientation parameters and orthorectification using a DEM [39]. We did not perform this processing, since the achieved accuracy is

quite sufficient for the correct visual identification of minor mud volcanic features. This is because an average diameter of such features is about 90 m (see Section 4).

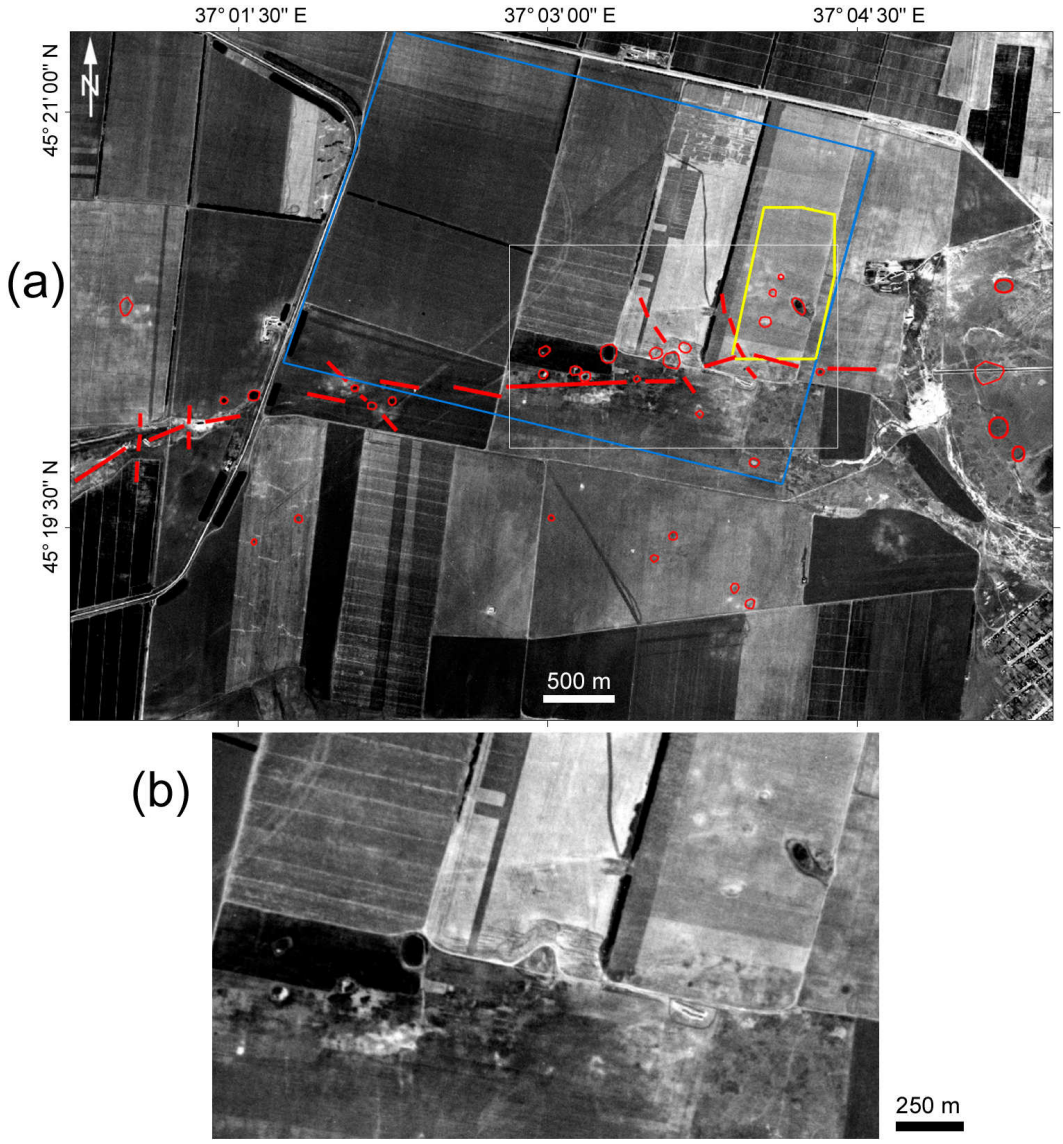

Figure 5. The study area: (**a**) The Corona image. Red lines and rings show detected lineaments and ring microstructures, correspondingly. The blue frame shows a territory under the unmanned aerial survey (see Section 3.3.1). The yellow frame shows the study site (see Figures 6 and 7). The white frame shows a zoomed-up portion of the image (see Figure 5b). (**b**) The zoomed-up portion of the Corona image. One can see ring microstructures delineated on (**a**). For the position of the study area, see Figure 1a, the yellow frame.

3.3. Local Level

At the local level, we utilized UAS-based data for a relatively small study site located within the study area (Figure 5a).

3.3.1. Field Works

In August 2018, an unmanned aerial survey was carried out in the central-northern part of the Taman Peninsula within the frameworks of the Bosporan Archaeological Expedition [40–43]. The main goal of the UAS survey was a comprehensive study of archaeological sites and the detection of hidden, partly buried archaeological features. Aerial survey and geomorphometric modeling are quite widely

used for predictive archaeological mapping [44–47]. To avoid misunderstanding, we should stress that the archaeological objects of the Taman Peninsula are buried by alluvial and, partly, colluvial sediments [48], and not by mud volcanic flows. Archaeological sites are just located next to mud volcanic formations in this region.

Within the study area, a territory measured about 3.25 km by 2.2 km including suspected minor mud volcanic formations (Figure 5a) was surveyed on 28 August 2018. We used a DJI Phantom 4 Pro [49], a multi-copter UAS equipped with a camera FC6310 (a focal length of 8.8 mm, a matrix of 5472 pixels × 3648 pixels with pixel sizes of 2.4 μm × 2.4 μm).

The weather was sunny during the flight. The air temperature ranged from 25 °C to 27 °C; the wind was southwest; the wind speed was 1 m/s at the flight altitude of 130 m above ground level.

The flights took about five hours. The aerial surveying consisted of 48 flight strips, including 3816 images. Forward and side overlaps were about 80% and 60%, correspondingly. Ground sample distance (GSD) was set to 3.2 cm per pixel.

For georeferencing, we used six targeted ground control points (GCPs). To measure their coordinates, we applied a Global Navigation Satellite System (GNSS) receiver Topcon Hiper (GPS/GLONASS, L1/L2).

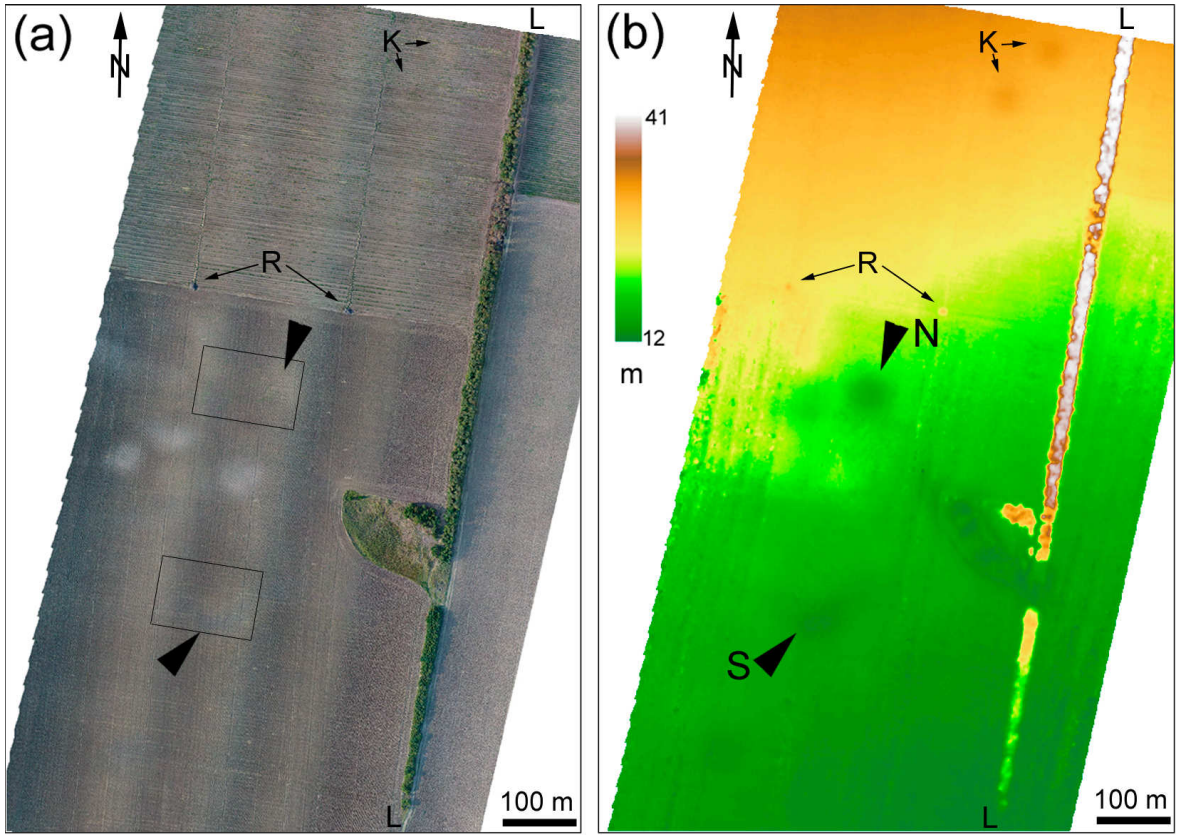

Figure 6. The study site: (**a**) UAS-based orthomosaic. Two black frames show the position of two images displayed in Figure 4c,d. (**b**) Elevation map. Two big arrows show the Northern (N) and Southern (S) ring microstructures detected by the geomorphometric analysis (see Figures 7 and 8). LL—a windbreak; R—mounds of agricultural refuse; K—probably, kurgans. For the position of the study site, see Figure 5a, the yellow frame.

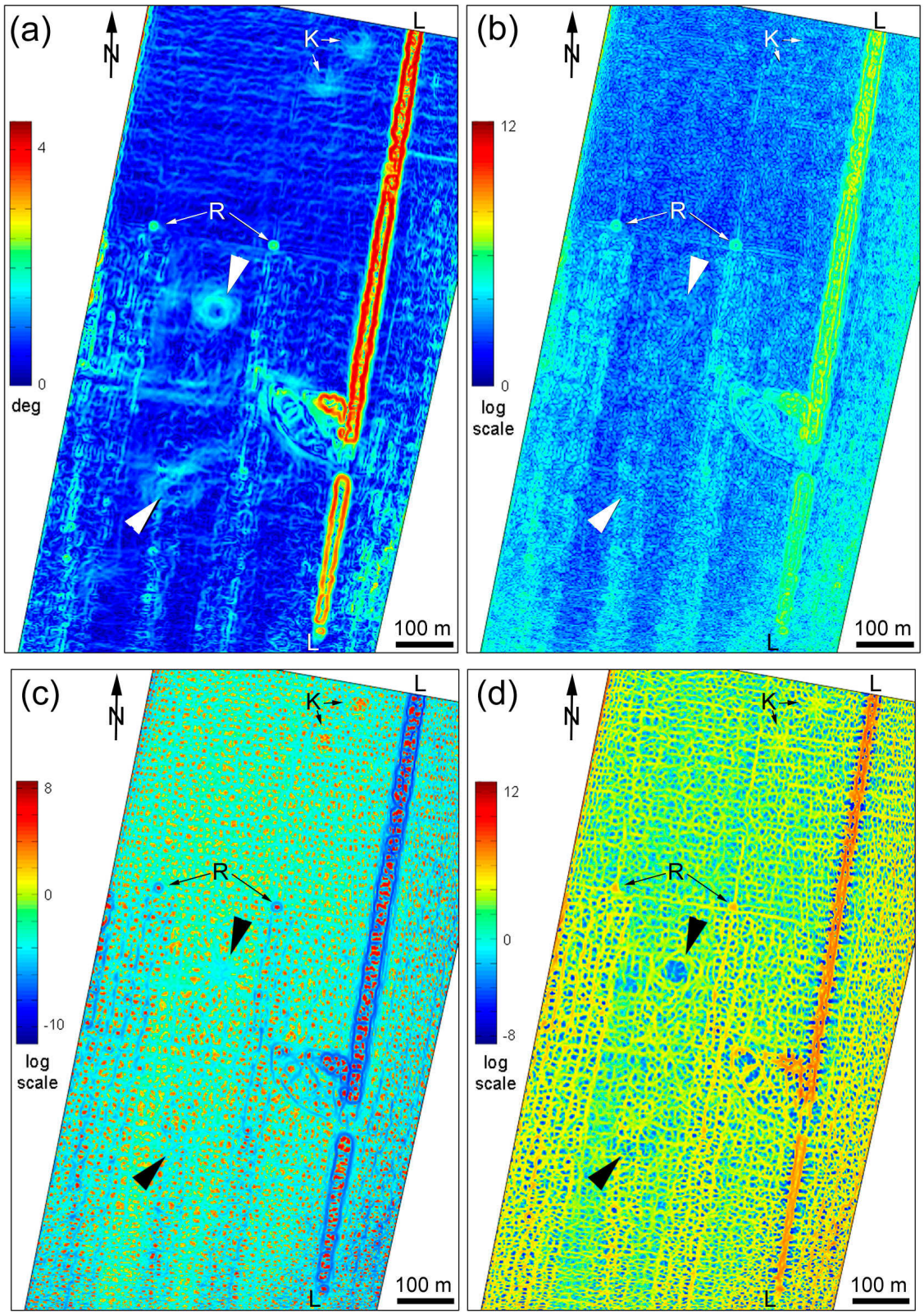

Figure 7. *Cont.*

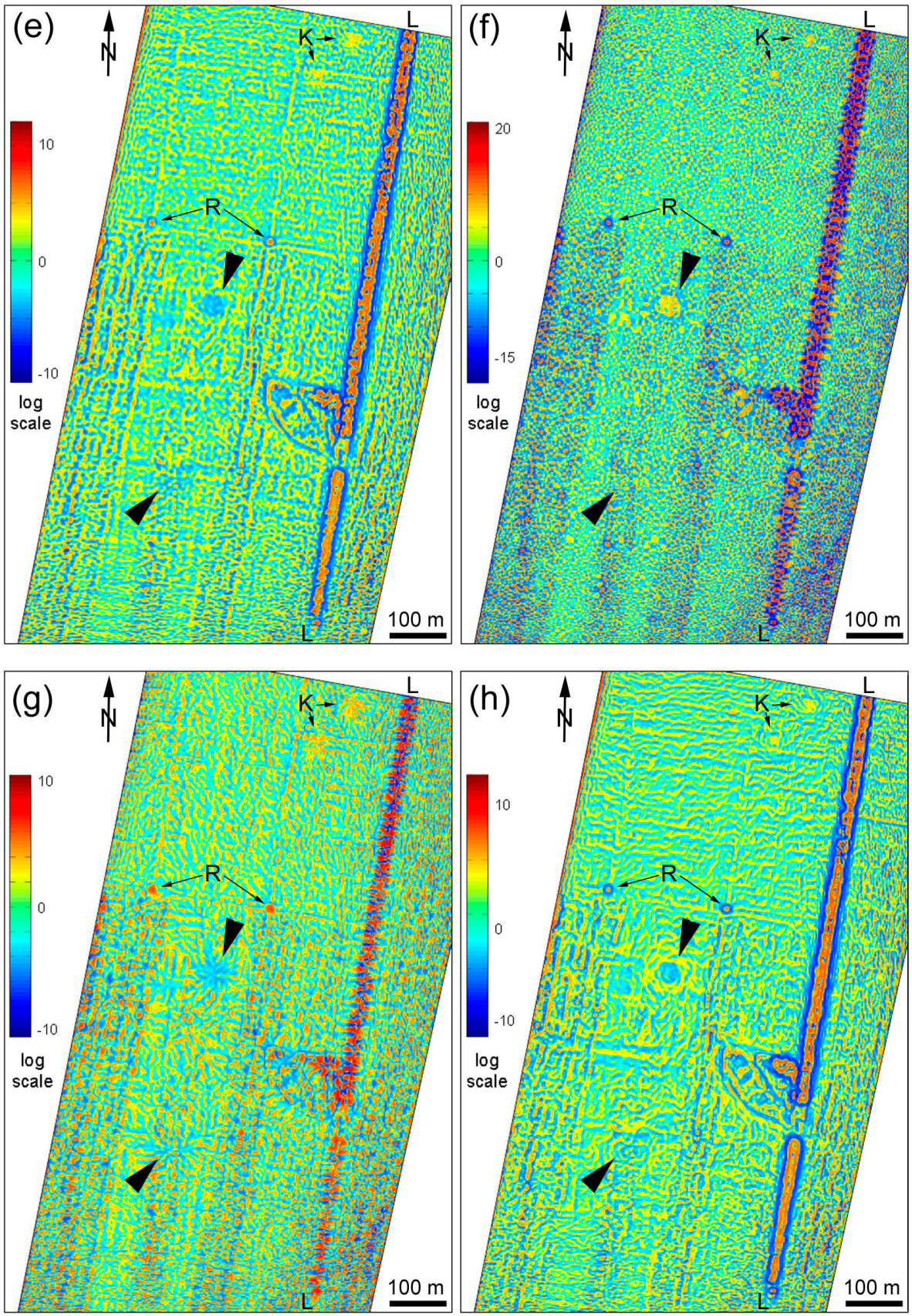

Figure 7. *Cont.*

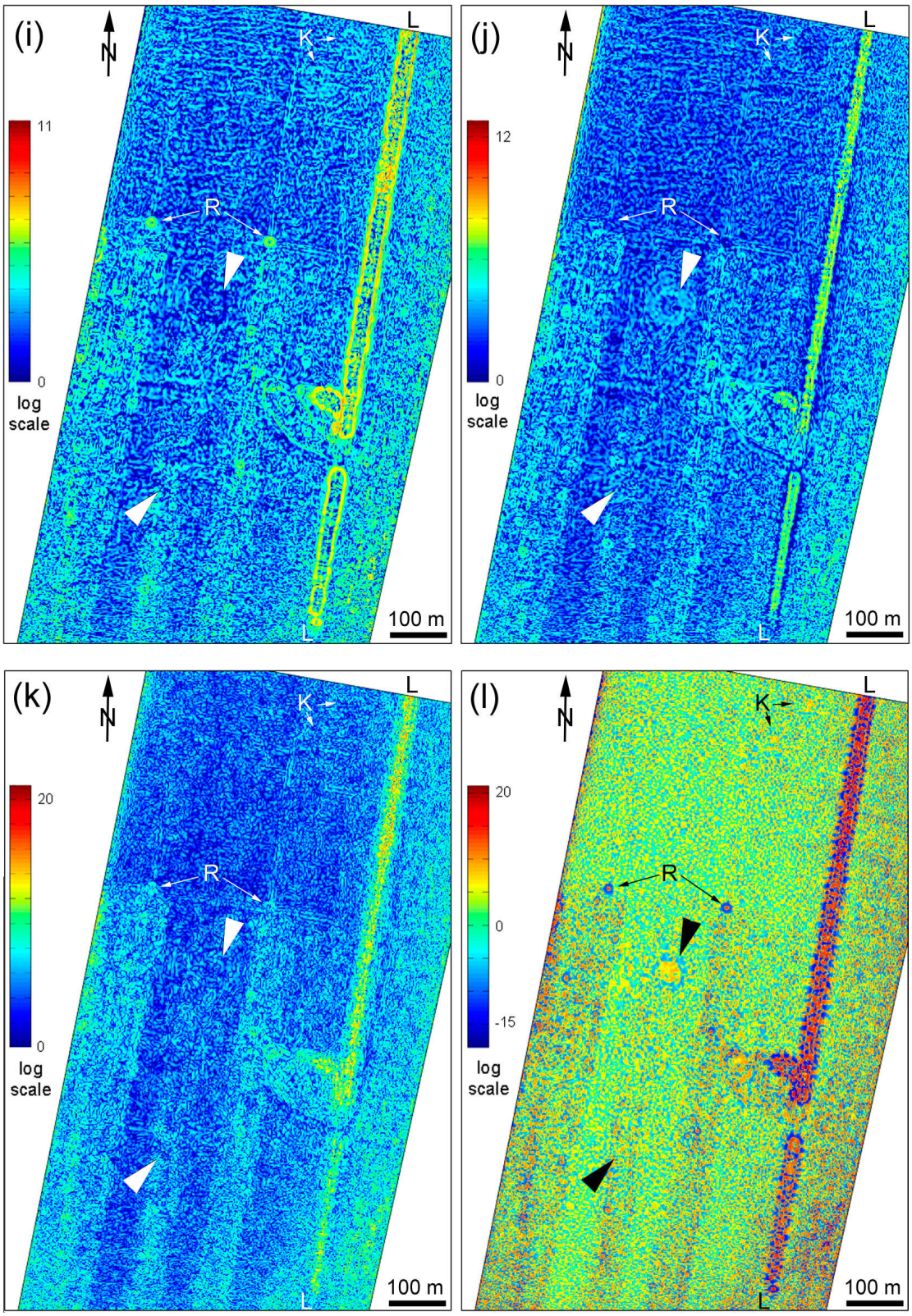

Figure 7. The study site, UAS-based morphometric maps: (**a**) slope; (**b**) unsphericity; (**c**) minimal curvature; (**d**) maximal curvature; (**e**) mean curvature; (**f**) Gaussian curvature; (**g**) horizontal curvature; (**h**) vertical curvature. (**i**) horizontal excess curvature; (**j**) vertical excess curvature; (**k**) ring curvature; and, (**l**) accumulation curvature. Two big arrows show the detected, Northern and Southern ring microstructures (see Figures 6 and 8). LL—a windbreak; R—agricultural refuse mounds; K—probably, kurgans. For the study site position, see Figure 5a, the yellow frame.

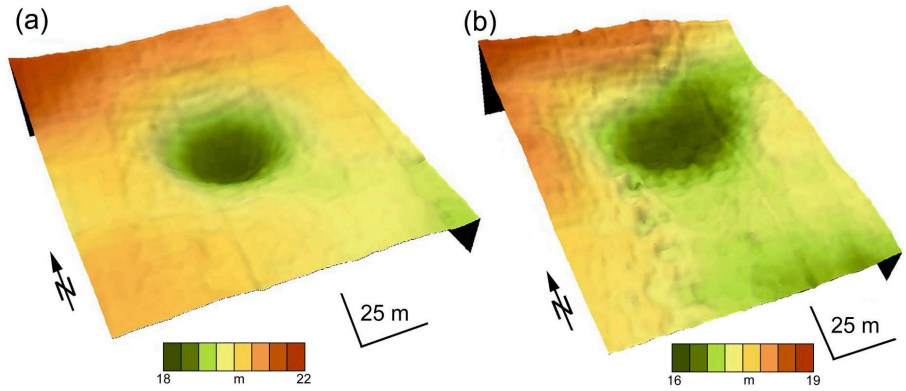

Figure 8. Three-dimensional models of the two ring microstructures detected by the geomorphometric analysis: (**a**) the Northern microstructure, (**b**) the Southern microstructure. 20× vertical scale exaggeration is used. For the microstructure locations, see Figure 6b.

3.3.2. Data Processing

We utilized Pinnacle software (Topcon Positioning Systems, Inc., Livermore, CA, USA) to process static sessions of satellite observations of GCPs coordinates.

The UAS imagery was photogrammetrically processed using Agisoft PhotoScan Professional 1.3.2 [50] including the following steps:

1. Aligning aerial images by the least-squares bundle adjustment with data from the camera self-calibration based on the GCP coordinates. The planimetric and vertical root mean square errors (RMSEs) of the aerial triangulation were 0.5 cm and 2.5 cm, correspondingly.
2. Building a dense point cloud by the Agisoft algorithm automatically matching tie points [51]. This algorithm belongs to the group of semi-global matching methods [52].
3. Generating a 1-m gridded DSM by the inverse distance weighted interpolation [53] of the dense point cloud.
4. Producing an orthomosaic with a resolution of 0.2 m.

For further work, we used portions of the obtained orthomosaic and DSM covering a selected study site measured approximately 1.2 km by 0.6 km (Figure 6). Within the study site, there were no GCPs, which could be used to estimate accuracy of this DSM. Thus, such estimation can be done indirectly. Indeed, it is known that a DSM/DEM RMSE ranges from two to four values of a GSD if a DSM/DEM was generated by a correct photogrammetric processing of images captured by various types of UASs, GCPs, and the calibration or self-calibration data [54]. Because GSD was 3.2 cm in this study (see Section 3.3.1), the DSM RMSE ranges from 6.4 cm to 12.8 cm.

We utilized the DSM with the resolution of 1 m for the following reasons: More detailed DSMs (e.g., 0.25-m or 0.5-m gridded ones) include a dense system of parallel patterns describing geometry of arable furrows (Figure 4c,d). These microtopographic patterns interfere with the visual perception of the study site topography, especially on morphometric maps (this is because morphometric calculations increase the manifestation of high-frequency components of a DEM/DSM). At the same time, the 1-m gridded DSM provides such a level of topographic generalization that 'neutralizes' this influence of furrows, while the 1-m resolution is enough to reveal minor mud volcanic features, with typical sizes ranging from 40 m to 100 m (see Section 4).

There is a vineyard in northern portion of the study site, a narrow windbreak crossing the site from north to south, and a small overgrown depression in its eastern part (Figure 6a). However, we did not construct a DEM from the DSM, because suspected minor mud volcanic features, which were found on the Corona image (Figure 5a), are located within the southern portion of the study site, which was ploughed and free from trees and grass cover during the survey (Figure 6a).

3.3.3. Geomorphometric Modeling

We derived models of 13 local morphometric variables from the UAS-based DSM. The list of morphometric variables included slope (G), minimal curvature (k_{min}), maximal curvature (k_{max}), mean curvature (H), Gaussian curvature (K), unsphericity (M), horizontal (or tangential) curvature (k_h), vertical (or profile) curvature (k_v), difference curvature (E), vertical excess curvature (k_{ve}), horizontal excess curvature (k_{he}), accumulation curvature (K_a), and ring curvature (K_r). Each of these variables has a clear physical and mathematical sense and describes a particular property of the surface; for their definitions, formulas, and interpretations, see [12,55,56] and (Table 1).

Table 1. Definitions and interpretations of local morphometric variables [12,55,56].

Variable, Notation, and Unit	Definition, Interpretation, and Formula
Slope, G, °	An angle between the tangential and horizontal planes at a given point of the surface. Relates to the velocity of gravity-driven flows.
Minimal curvature, k_{min}, m^{-1}	A curvature of a principal section with the lowest value of curvature at a given point of the surface. $k_{min} > 0$ corresponds to hills, while $k_{min} < 0$ relates to valleys.
Maximal curvature, k_{max}, m^{-1}	A curvature of a principal section with the highest value of curvature at a given point of the surface. $k_{max} > 0$ corresponds to ridges, while $k_{max} < 0$ relates to closed depressions.
Mean curvature, H, m^{-1}	A half-sum of curvatures of any two orthogonal normal sections at a given point of the surface. H represents two accumulation mechanisms of gravity-driven substances—convergence and relative deceleration of flows—with equal weights.
Gaussian curvature, K, m^{-2}	A product of maximal and minimal curvatures. K retains values in each point of the surface after its bending without breaking, stretching, and compressing.
Unsphericity, M, m^{-1}	A half-difference of maximal and minimal curvatures. $M = 0$ on a sphere; M values show the extent to which the shape of the surface is non-spherical at a given point.
Horizontal (or tangential) curvature, k_h (m^{-1})	A curvature of a normal section tangential to a contour line at a given point of the surface. k_h is a measure of flow convergence and divergence. Gravity-driven lateral flows converge where $k_h < 0$, and diverge where $k_h > 0$. k_h reveals ridge and valley spurs.
Vertical (or profile) curvature, k_v (m^{-1})	A curvature of a normal section having a common tangent line with a slope line at a given point of the surface. k_v is a measure of relative deceleration and acceleration of gravity-driven flows. They are decelerated where $k_v < 0$, and are accelerated where $k_v > 0$. k_v mapping allows revealing terraces and scarps.
Difference curvature, E, m^{-1}	A half-difference of vertical and horizontal curvatures. Comparing two accumulation mechanisms of gravity-driven substances, E shows to what extent the relative deceleration of flows is higher than flow convergence at a given point of the surface.
Horizontal excess curvature, k_{he}, m^{-1}	A difference of horizontal and minimal curvatures. k_{he} shows to what extent the bending of a normal section tangential to a contour line is larger than the minimal bending at a given point of the surface.
Vertical excess curvature, k_{ve}, m^{-1}	A difference of vertical and minimal curvatures. k_{ve} shows to what extent the bending of a normal section having a common tangent line with a slope line is larger than the minimal bending at a given point of the surface.
Accumulation curvature, K_a, m^{-2}	A product of vertical and horizontal curvatures. A measure of the extent of flow accumulation at a given point of the surface.
Ring curvature, K_r, m^{-2}	A product of horizontal excess and vertical excess curvatures. Describes flow line twisting.

We applied the large set of variables, rather than particular ones, because it was unclear how hidden mud volcanic features are reflected in the land surface.

Morphometric models were produced by the universal spectral analytical method [57]. The method is intended for the processing of regularly spaced DEMs/DSMs within a single framework, which includes DEM/DSM global approximation, denoising, generalization, and calculating the partial derivatives of elevation. The method is based on high-order orthogonal expansions using the Chebyshev polynomials with the subsequent Fejér summation.

We used 500 expansion coefficients of the original elevation function by the Chebyshev polynomials by both X- and Y-axes. Such a number of expansion coefficients made it possible to remove high-frequency noise from the DSM without losing important details.

Curvatures have wide dynamic ranges. One should logarithmically transform morphometric models with the following expression to avoid a loss of information on curvature value distribution in mapping [12,55,56]:

$$\Theta' = \text{sign}(\Theta) \ln(1 + 10^n |\Theta|) \quad (1)$$

where Θ and Θ' are an initial and transformed values of a morphometric variable, respectively; $n = 0$ for elevation and nonlocal variables, $n = 2, \ldots, 18$ for local variables. The selection of the n value depends on the DEM resolution. We used $n = 4$ for curvature mapping. The computational boundary effects were removed. The obtained morphometric maps (Figure 7) have the resolution of 1 m.

The geomorphometric modeling was conducted with Matlab R2008b software.

For specialties of geomorphometric studies that are based on data from unmanned aerial surveys, see also [58].

3.4. GIS-Based Analysis

All of the obtained materials were exported into MapInfo Pro 16.0 software for co-registration, visualization, and analysis.

The peculiarities and accuracy of the Corona image registration is described in detail in Section 3.2. In order to assess the mutual registration accuracy of AW3D30- and UAS-based DSMs, we used matrix subtraction, that is, the UAS-based DSM was subtracted from the AW3D30-based DSM. The sample size was 1247 points. The mean elevation difference between two DSMs was −1.7 m with the standard deviation of 1.9 m. This indirectly indicates the rather high accuracy of the AW3D30 DSM for the Taman Peninsula in comparison with other territories [30,32].

Finally, the AW3D30-based hill-shading map and the Corona image were visually analyzed to determine key tectonic structural elements of the study area at the regional (Figure 1b) and sub-regional levels (Figure 5a). Minor, weakly topographically expressed mud volcanic structures were detected on the Corona image (Figure 5a) and the UAS-based morphometric maps (Figure 7). Three-dimensional (3D) models of geomorphometrically found ring microstructures (Figure 8) were also constructed for better understanding their geometry.

4. Results

At the regional level, on the AW3D30-based hill-shaded map (Figure 1b), one can clearly see topographically manifested folded structures—anticlines and synclines—of the Taman Peninsula (see Section 2). Anticlines correspond to narrow, north-east-, and almost west-east-striking ridges, while synclines correlate with wide, interridge valleys, and depressions. Large, recently active mud volcanic structures are also clearly visible on the hill-shaded map (Figure 1b). They are manifested as characteristic 'pimples' located along the anticline axes.

At the subregional level, the analysis of the Corona image allowed us to detect a series of almost west-east-striking lineaments (Figure 5a). These features correspond to the axis of the syncline located between the Fontalovskaya and Anastasievskaya–Krasnodar anticlines. Apparently, these lineaments indicate a fracture zone of the current tectonic deformations. In the syncline center, we detected lineaments probably reflecting left strike-slip displacements, which are transverse to the syncline axis.

One can also observe a series of ring microstructures with diameters that range from 40 m to 100 m located along the syncline axial zone (Figure 5a).

At the local level, the morphometric maps (Figure 7) also allowed us to detect ring microstructures as well as to study their geometry and topographic expression in more details. Maps of all morphometric variables display ring microstructures, since they are reflected in the land surface. However, different variables have different abilities to detect the microstructures, because topographic features are described by a particular morphometric variable according to its physical, mathematical, and geomorphic sense (Table 1) [12]. We found that ring microstructures are best detected by slope, horizontal, and vertical curvatures (Figure 7a,g,h).

The geometry of the detected ring microstructures can be clarified using 3D models of two typical ones (Figure 8). The Northern ring microstructure (Figure 8a) has a regular, almost ideally ring shape with a diameter of 80 m and an average depth of about 2 m. The depression walls have different heights: its south-eastern walls lower than the north-western ones by 1 m. The depression walls have a similar slope not exceeding 4°.

The Southern ring microstructure (Figure 8b) has a complex, bean-like shape elongated from south-west to north-east. Its long and short side lengths are 120 m and 80 m, correspondingly. The microstructure has the flat bottom about 25 m long and 10–13 m wide. Its south-eastern part is 1 m lower than the north-western one. The north-eastern wall of the depression is flatter. The opposite walls of this depression are symmetrical. For the cross-sections along the short and long sides, the slope does not exceed 3° and 2°, correspondingly.

5. Discussion

The multiscale analysis of the remote sensing and morphometric data allowed us to obtain new information clarifying the conditions of neotectonic development in the central-northern margin of the Taman Peninsula. The use of three scale levels allowed analyzing the data from general to specific. In particular, using the Corona satellite photograph, we detected ring microstructures, which are similar in appearance and observed over the relatively vast area concentrating along the syncline axis. These facts suggested that the formation of the microstructures was not accidental. At the same time, the Corona image could not provide us with visual and numerical information either describing topographic properties of the landscape or reflecting regional tectonic structure. The freely distributed, quasi-global terrain model AW3D30 DSM was used for solving the latter task. However, the AW3D30 DSM resolution of one arc-second does obviously not allow one to perform geomorphometric modeling of the microtopography. Therefore, to quantitatively analyze the ring microstructures, it was optimal to obtain the new, high-resolution DSM and accurate orthomosaic using materials from the recent unmanned aerial survey. Utilizing these data, we were able to clarify the spatial position and shape of the selected ring microstructures, as well as to carry out their geomorphometric analysis.

Three morphometric variables—slope, horizontal, and vertical curvatures (Figure 7a,g,h)—describe well both convex and concave microtopographic closed forms. For example, convex microbreakes revealed by the vertical curvature can be used to clarify outer limits of the ring microstructures (Figure 7h). The slope map shows the slope asymmetry of the ring microstructures (Figure 7a). Using this information in combination with microflow patterns revealed by the horizontal curvature (Figure 7g), one may estimate the dynamics and direction of erosion processes that are hidden by plowing at the study site. Other calculated morphometric variables (Figure 7b–f, i–l) showed worse results than those three ones in terms of visualization of minor, partly hidden ring microstructures.

The development of the tectonic deformation zone within the syncline axis between the Fontalovskaya and Anastasievskaya–Krasnodar anticlines (Figure 1b) was probably accompanied by active mud volcanism. It reached the highest intensity in the eastern part of the syncline, where the large mud volcano, Akhtanizovskaya Sopka formed (Figure 1a). Therefore, a series of concave ring microstructures (Figure 5a) can be interpreted as the result of mud volcanic eruption and degassing. In synclines of the Kerch–Taman mud volcanic province, minor forms of mud volcanism are represented

by small gryphons and salses [4]. Thus, the detected ring microstructures are likely to be minor inactive mud volcanic features, which were ploughed and covered by soil. It is also possible that the ring microstructures are associated with mud volcanic focuses located within anticlines, because large mud volcanoes (e.g., West and East Tsymbals, Akhtanizovskaya Sopka, Boris and Gleb, and others (Figure 1a)) are situated around the study area. The occurrence of the microstructures in the synclinal zone became possible due to the presence of numerous north-west-striking fracture zones, complicating this area.

Diapirism, which is associated with development of mud volcanism, is usually initiated by a general increase in the tectonic activity of a region. In the Kerch–Taman mud volcanic province, there is a clear spatial orientation of folds and faults. In the south-western part of the Taman Peninsula, north-east-striking folds dominate. This reflects the influence of the Crimean Orogen and the Kerch–Taman transverse trough (Figure 2). The influence of the orogen of the Great Caucasus is reflected in a combination of almost west-east-striking folds and faults with north-west-striking ones. Less expressive, transverse flexural and rupture zones were also established in the tectonic structure of the Taman Peninsula. As a structural element of the interpericlinal zone between the Crimean and Great Caucasian orogens (Figure 2), recent folds were formed under conditions of the horizontal compression. The presence of the thick clayey Maikop strata led to the widespread development of the Maikop clay diapirism in this region. As a result, the majority of anticlines are 'active', growing, relatively narrow, linear diapirs. They divide relatively 'passive', simply constructed, wide synclines [59]. At the same time, sediments are actively accumulated in the synclines contributing to an increase in pressure on the Maikop clays extruded in the anticlines [60].

In the Taman anticline cores, the Supra-Maikop Upper Miocene and Lower Pliocene deposits are exposed, while the Maikop strata are just starting to crop out in the cores of some diapiric folds. The wide synclines are formed by the Akchagyl and Quaternary deposits, as well as occupied by vast estuaries [59].

The beginning of the diapir formation dates back to the Early–Middle Miocene. By the Late Miocene, the major anticlinal zones had already been established and mud volcanic activity was manifested, as evidenced by the presence of buried hill breccia in the Sarmatian deposits around the Dubovy Rynok, Strelchanskaya, Bely Khutor, and other mud volcanoes (Figure 1a). However, the most intense folding occurred in the Pliocene–Quaternary; it formed the recent structure of the upper structural floor [61]. The development of the tectonic deformation zones associated with diapirism as well as activation of the seismogenic events may have caused formation of the inter-anticlinal mud volcanic fields expressed by numerous ring microstructures. For the Great Caucasus and Crimea in the Middle Pliocene, the shift of the stress field and reorientation of the near-west-east compression to the near-north-south one [62] changed the manifestation mode of the mud volcanism. Probably, from this moment, the regional mud volcanism is actively manifested in intersection nodes of the major anticlinal mud volcanic zones, which correspond to the systems of almost west-east-striking structures and north-west-striking ones [63].

We proposed a scheme for the generation of mud volcanoes in the Kerch–Taman mud volcanic province (Figure 9) [64]. The major generation zones are latitudinal compression structures that are primarily caused by discontinuities of the basement (that is, a conditional level related to pre-Maikop deposits).

In these compression zones, the conditions of strong compression deformations arise contributing to the formation of clay diapirs. The strain distribution is not uniform. Particularly strong fluctuations arise at the intersection nodes of latitudinal compression zones with transverse zones of other kinematics (e.g., shear and extension zones). At the intersection nodes, decompression conditions arise and clay liquefaction occurs, which leads to the formation of hill breccia. There are many clayey interlayers in the Maikop deposits contributing to the formation of numerous detachment faults (Figure 9). All of this complicates the situation and leads to the formation of complex branching channels and the development of additional mud volcanic structures.

The process occurs impulsively, leading to the formation of conical structures at the stage of active development of mud volcanic focuses, as well as subsidence and collapse structures (i.e., depressed synclines and lacustrine basins) at the stage of devastation of those focuses (Figure 9).

The approach utilized in this study can enrich a toolbox of researchers using remote sensing data, particularly UAS-based imagery, for studying mud volcanism. Indeed, few people are engaged in identifying and studying minor, inactive mud volcanic features, although information on their spatial distribution can clarify regional tectonic and mud volcanic activity in the geologically recent past. As far as we know, mud volcanologists do not use geomorphometric modeling, although geomorphometry has taken a firm place in various geosciences [12,65,66]. A three-level multiscale analysis is generally rarely used in studies based on remote sensing data: one or two scale levels are much more popular within a framework of a single study.

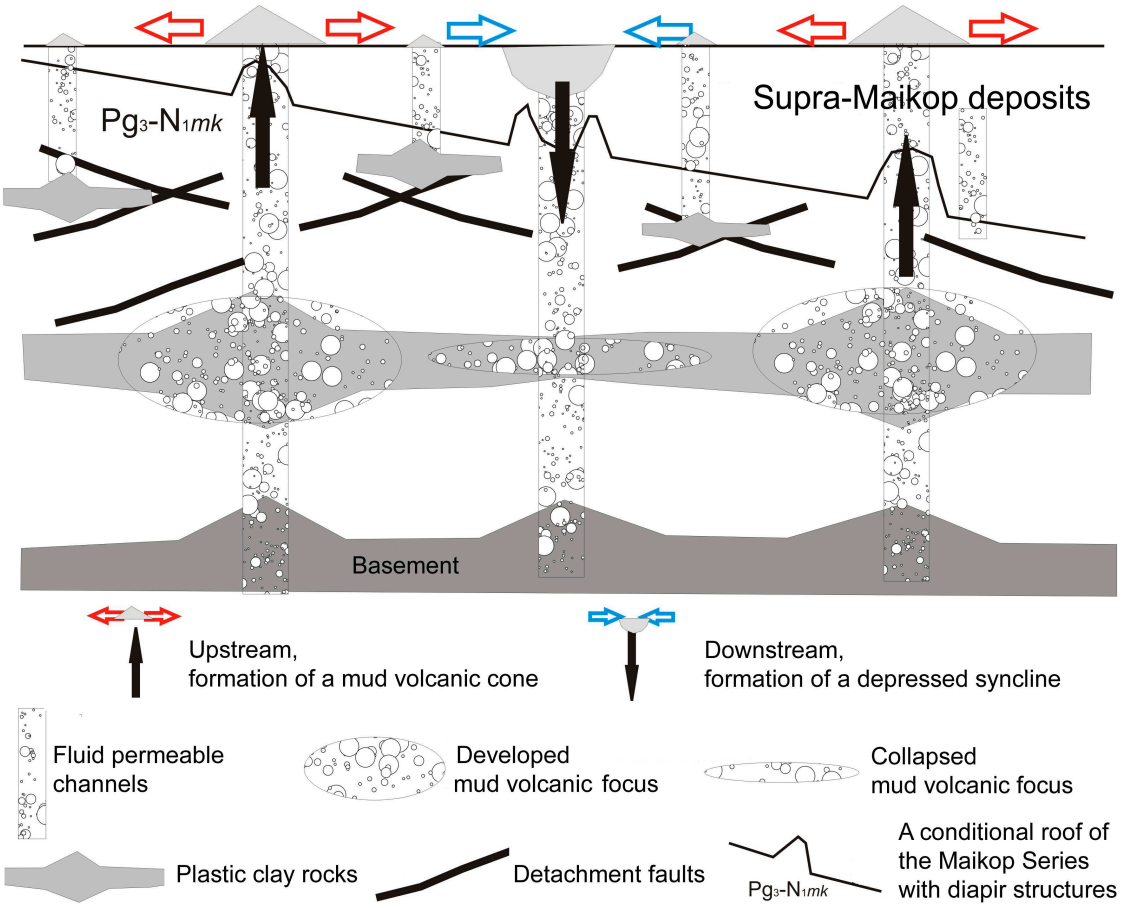

Figure 9. A scheme for the generation of mud volcanoes in the Kerch–Taman mud volcanic province.

For the detection of minor mud volcanic features at the Taman Peninsula, German military aerial photographs can possibly be useful. This is because these images were captured during the Second World War, that is, before agricultural modification of the Taman landscapes. The Luftwaffe aerial photographs are now stored in Russian and U.S. archives, and they are conditionally available for research [67]. These images may probably be considered a source for photogrammetric generation of rather detailed DEMs and further geomorphometric analysis of the entire territory of the Kerch–Taman mud volcanic province.

6. Conclusions

In this study, we demonstrated the possibility of the use of heterogeneous, multiscale, and multitemporal remote sensing and morphometric data for searching and analyzing minor,

geological ring structures. This task was solved by a combined analysis of the quasi-global AW3D30 DSM, the Corona historical satellite image, and the recent UAS-based DSM. All of the data were transformed into a unified coordinate system and co-registered in a GIS. The accuracy of the data registration at all levels made it possible to obtain reliable results on the spatial position of small ring landforms. The AW3D30 DSM-based hill-shaded map displayed the general scene of the topographically manifested, regional fold tectonics responsible for mud volcanism in the Taman Peninsula. In the Corona images, we were able to see the number, spatial distribution peculiarities, and typical sizes of the ring microstructures. The geomorphometric analysis of the UAS-based DSM allowed us to perform a thorough assessment of the selected microstructures. It should be emphasized that none of the used sources is individually self-sufficient for such research.

In the geological context, the combined multiscale analysis of remote sensing and morphometric data allowed us to reveal the hidden remains of mud volcanism for the central-northern part of the Taman Peninsula, as well as to obtain new information clarifying peculiarities of the neotectonic development in this region. The development of the tectonic deformation focus within the syncline axis between the Fontalovskaya and Anastasievskaya–Krasnodar anticlines was probably accompanied by active mud volcanism. It reached its highest intensity in the eastern part of the syncline, where the large mud volcano Akhtanizovskaya Sopka formed.

Author Contributions: Conceptualization, T.N.S.; methodology, T.N.S.; validation, T.N.S. and I.V.F.; formal analysis, T.N.S. and I.V.F.; investigation, T.N.S., I.V.F., and D.E.B.; resources, T.N.S. and O.V.G.; data curation, T.N.S., and I.V.F.; writing, I.V.F., T.N.S., D.E.B. and O.V.G.; visualization, T.N.S., I.V.F. and O.V.G.; supervision, I.V.F. All authors have read and agreed to the published version of the manuscript.

Funding: This research received no external funding.

Conflicts of Interest: The authors declare no conflict of interest.

References

1. Dimitrov, I.L. Mud volcanoes—The most important pathway for degassing deeply buried sediments. *Earth Sci. Rev.* **2002**, *59*, 49–76. [CrossRef]
2. Kopf, A.J. Significance of mud volcanism. *Rev. Geophys.* **2002**, *40*, 1–52. [CrossRef]
3. Mazzini, A.; Etiope, G. Mud volcanism: An updated review. *Earth Sci. Rev.* **2017**, *168*, 81–112. [CrossRef]
4. Shnyukov, Y.F.; Sheremetyev, V.M.; Maslakov, N.A.; Kutny, V.A.; Gusakov, I.N.; Trofimov, V.V. *Mud Volcanoes of the Kerch–Taman Region*; GlavMedia: Krasnodar, Russia, 2006; 174p. (In Russian)
5. Shnyukov, Y.F.; Aliyev, A.A.; Rahmanov, R.R. Mud volcanism of Mediterranean, Black and Caspian seas: Specificity of development and manifestations. *Geol. Miner. Resour. World Ocean* **2017**, *13*, 5–25. [CrossRef]
6. Sobisevich, A.L.; Sobisevich, L.E.; Tveritinova, T.Y. On mud volcanism in the Late Alpine folded edifice of the North-Western Caucasus (Exemplified by the study of the deep structure of the Shugo Mud Volcano). *Geol. Miner. Resour. World Ocean* **2014**, *36*, 80–93, (In Russian, with English Abstract).
7. Tveritinova, T.Y.; Sobisevich, A.L.; Sobisevich, L.E.; Likhodeev, D.V. Structural position and structure peculiarities of the Mount Karabetov Mud Volcano. *Geol. Miner. Resour. World Ocean* **2015**, *40*, 106–122. (In Russian, with English Abstract).
8. Podymov, I.S. A map of mud volcanoes of the Taman Peninsula. In *Research and Monitoring of Mud Volcanism of Taman in the Context of the Modern Problem of Ecological Safety for the Azov-Black Sea Coast of Russia*; Southern Branch, Shirshov Institute of Oceanology, Russian Academy of Science: Gelendzhik, Russia, 2015; Available online: https://mud-volcano.coastdyn.ru/map.html (accessed on 6 November 2020). (In Russian)
9. Trifonov, V.G.; Makarov, V.I.; Safonov, Y.G.; Florensky, P.V. (Eds.) *Space Remote Sensing Data in Geology*; Nauka: Moscow, Russia, 1983; 535p, (In Russian, with English Contents).
10. Scanvic, J.-Y. *Aerospatial Remote Sensing in Geology*; Balkema: Rotterdam, The Netherlands, 1997; 280p.
11. Gupta, R.P. *Remote Sensing Geology*, 2nd ed.; Springer: Berlin, Germany, 2003; 655p.
12. Florinsky, I.V. *Digital Terrain Analysis in Soil Science and Geology*; Elsevier: Amsterdam, The Netherlands, 2016; p. 486.
13. Colomina, I.; Molina, P. Unmanned aerial systems for photogrammetry and remote sensing: A review. *ISPRS J. Photogramm. Remote Sens.* **2014**, *92*, 79–97. [CrossRef]

14. Shahbazi, M.; Théau, J.; Menard, P. Recent applications of unmanned aerial imagery in natural resource management. *GISci. Remote Sens.* **2014**, *51*, 339–365. [CrossRef]
15. Whitehead, K.; Hugenholtz, C.H. Remote sensing of the environment with small unmanned aircraft systems (UASs), part 1: A review of progress and challenges. *J. Unmanned Veh. Syst.* **2014**, *2*, 69–85. [CrossRef]
16. Whitehead, K.; Hugenholtz, C.H.; Myshak, S.; Brown, O.; LeClair, A.; Tamminga, A.; Barchyn, T.E.; Moorman, B.; Eaton, B. Remote sensing of the environment with small unmanned aircraft systems (UASs), part 2: Scientific and commercial applications. *J. Unmanned Veh. Syst.* **2014**, *2*, 86–102. [CrossRef]
17. Pajares, G. Overview and current status of remote sensing applications based on unmanned aerial vehicles (UAVs). *Photogramm. Eng. Remote Sens.* **2015**, *81*, 281–330. [CrossRef]
18. Bhardwaj, A.; Sam, L.; Akanksha; Martín-Torres, F.J.; Kumar, R. UAVs as remote sensing platform in glaciology: Present applications and future prospects. *Remote Sens. Environ.* **2016**, *175*, 196–204. [CrossRef]
19. Toth, C.K.; Jóźków, G. Remote sensing platforms and sensors: A survey. *ISPRS J. Photogramm. Remote Sens.* **2016**, *115*, 22–36. [CrossRef]
20. Woodget, A.S.; Austrums, R.; Maddock, I.P.; Habit, E. Drones and digital photogrammetry: From classifications to continuums for monitoring river habitat and hydromorphology. *Wiley Interdiscip. Rev. Water* **2017**, *4*, e1222. [CrossRef]
21. Singh, K.K.; Frazier, A.E. A meta-analysis and review of unmanned aircraft system (UAS) imagery for terrestrial applications. *Int. J. Remote Sens.* **2018**, *39*, 5078–5098. [CrossRef]
22. Xiang, T.-Z.; Xia, G.-S.; Zhang, L. Mini-unmanned aerial vehicle-based remote sensing: Techniques, applications, and prospects. *IEEE Geosci. Remote Sens. Mag.* **2019**, *7*, 29–63. [CrossRef]
23. Santagata, T. Monitoring of the Nirano Mud Volcanoes Regional Natural Reserve (North Italy) using unmanned aerial vehicles and terrestrial laser scanning. *J. Imaging* **2017**, *3*, 42. [CrossRef]
24. Di Felice, F.; Mazzini, A.; Di Stefano, G.; Romeo, G. Drone high resolution infrared imaging of the Lusi mud eruption. *Mar. Pet. Geol.* **2018**, *90*, 38–51. [CrossRef]
25. Di Stefano, G.; Romeo, G.; Mazzini, A.; Iarocci, A.; Hadi, S.; Pelphrey, S. The Lusi drone: A multidisciplinary tool to access extreme environments. *Mar. Pet. Geol.* **2018**, *90*, 26–37. [CrossRef]
26. Blagovolin, N.S. *Geomorphology of the Kerch–Taman Region*; Soviet Academic Press: Moscow, Russia, 1962; 201p. (In Russian)
27. Gaydalenok, O.V. Structure of the Kerch-Taman Zone of Folded Deformations of the Azov-Kuban Trough. Ph.D. Thesis, Geological Institute, Russian Academy of Sciences, Moscow, Russia, 2020; 128p. (In Russian).
28. Trifonov, V.G.; Sokolov, S.Y.; Sokolov, S.A.; Hessami, K. Mesozoic–Cenozoic Structure of the Black Sea–Caucasus–Caspian Region and Its Relationships with the Upper Mantle Structure. *Geotectonics* **2020**, *54*, 331–355. [CrossRef]
29. Tadono, T.; Nagai, H.; Ishida, H.; Oda, F.; Naito, S.; Minakawa, K.; Iwamoto, H. generation of the 30 m-mesh global digital surface model by ALOS PRISM. *ISPRS Int. Arch. Photogramm. Remote Sens. Spat. Inf. Sci.* **2016**, *41*, 157–162. [CrossRef]
30. Florinsky, I.V.; Skrypitsyna, T.N.; Luschikova, O.S. Comparative accuracy of the AW3D30 DSM, ASTER GDEM, and SRTM1 DEM: A case study on the Zaoksky Testing Ground, Central European Russia. *Remote Sens. Lett.* **2018**, *9*, 706–714. [CrossRef]
31. Pavlova, A.I.; Pavlov, A.V. Analysis of correction methods for digital terrain models based on satellite data. *Optoelectron. Instrum. Data Process.* **2018**, *54*, 445–450. [CrossRef]
32. Florinsky, I.V.; Skrypitsyna, T.N.; Trevisani, S.; Romaikin, S.V. Statistical and visual quality assessment of nearly-global and continental digital elevation models of Trentino, Italy. *Remote Sens. Lett.* **2019**, *10*, 726–735. [CrossRef]
33. ALOS Global Digital Surface Model "ALOS World 3D–30m" (AW3D30). Available online: http://www.eorc.jaxa.jp/ALOS/en/aw3d30/ (accessed on 1 November 2019).
34. Horn, B. Hill shading and the reflectance map. *Proc. IEEE* **1981**, *69*, 14–47. [CrossRef]
35. Schowengerdt, R.A.; Glass, C.E. Digitally processed topographic data for regional tectonic evaluations. *GSA Bull.* **1983**, *94*, 549–556. [CrossRef]
36. Chorowicz, J.; Dhont, D.; Gündoğdu, N. Neotectonics in the eastern North Anatolian fault region (Turkey) advocates crustal extension: Mapping from SAR ERS imagery and digital elevation model. *J. Struct. Geol.* **1999**, *21*, 511–532. [CrossRef]

37. Earth Resources Observation and Science (EROS) Center. *Declassified Satellite Imagery—1*; U.S. Geological Survey: Sioux Fall, SD, USA, 1995. [CrossRef]
38. Kraus, K. *Photogrammetry: Geometry from Images and Laser Scans*, 2nd ed.; de Gruyter: Berlin, Germany, 2007; 459p.
39. Casana, J.; Cothren, J. Stereo analysis, DEM extraction and orthorectification of Corona satellite imagery: Archaeological applications from the Near East. *Antiquity* **2008**, *82*, 732–749. [CrossRef]
40. Kurkov, V.M.; Skripitsina, T.N.; Zhuravlev, D.V.; Schlotzhauer, U.; Kobzev, A.A.; Knyaz, V.A.; Mischka, C. Comprehensive survey of archaeological sites by ground and aerial remote sensing techniques. In *Ecology, Economy, Informatics*; Matishov, G.G., Ed.; Southern Federal University Publishers: Rostov on Don, Russia, 2018; Volume 3, pp. 151–158, (In Russian, with English Abstract). [CrossRef]
41. Zhuravlev, D.V.; Batasova, A.V.; Schlotzhauer, U.; Kurkov, V.M.; Skrypitsyna, T.N.; Knyaz, V.A.; Kudryashova, A.I.; Kobzev, A.A.; Mischka, C. New data on the structure of ancient monuments of the Asian Bosporus (from remote sensing data). In *XX Bosporan Readings: Cimmerian Bosporus and the World of the Barbarians in Antiquity and the Middle Ages*; Main Results and Prospects of Research; Zinko, V.N., Zinko, E.A., Eds.; Vernadsky Crimean Federal University: Simferopol, Russia, 2019; pp. 193–200. (In Russian)
42. Skrypitsyna, T.N.; Kurkov, V.M.; Kobzev, A.A.; Zhuravlev, D.V. Remote sensing data as a geospatial basis for archaeological research. *Eng. Surv.* **2019**, *13*, 18–26. (In Russian) [CrossRef]
43. Skrypitsyna, T.; Kurkov, V.; Zhuravlev, D.; Knyaz, V.; Batasova, A. Study of the hidden ancient anthropogenic landscapes using digital models of microtopography. *Proc. SPIE* **2020**, *11533*, 115331F. [CrossRef]
44. Verhagen, P.; Drăguţ, L. Object-based landform delineation and classification from DEMs for archaeological predictive mapping. *J. Archaeol. Sci.* **2012**, *39*, 698–703. [CrossRef]
45. Campana, S. Drones in archaeology. State-of-the-art and future perspectives. *Archaeol. Prospect.* **2017**, *24*, 275–296. [CrossRef]
46. Davis, D.S. Object-based image analysis: A review of developments and future directions of automated feature detection in landscape archaeology. *Archaeol. Prospect.* **2019**, *26*, 155–163. [CrossRef]
47. Luo, L.; Wang, X.; Guo, H.; Lasaponara, R.; Zong, X.; Masini, N.; Wang, G.; Shi, P.; Khatteli, H.; Chen, F.; et al. Airborne and spaceborne remote sensing for archaeological and cultural heritage applications: A review of the century (1907–2017). *Remote Sens. Environ.* **2019**, *232*, 111280. [CrossRef]
48. Trebeleva, G.V.; Gorlov, Y.V. Cultural landscape of the Taman Peninsula in ancient times. *Reg. Envir. Issues* **2019**, *1*, 39–46, (In Russian, with English Abstract). [CrossRef]
49. DJI Phantom 4. Available online: https://www.dji.com/phantom-4/info (accessed on 1 November 2019).
50. Agisoft LLC. *Agisoft PhotoScan User Manual: Professional Edition, Version 1.3*; Agisoft LLC: St. Petersburg, Russia, 2017; 105p.
51. Semenov, A.E.; Kryukov, E.V.; Rykovanov, D.P.; Semenov, D.A. Practical application of computer vision techniques to solve problems of recognition, 3D reconstruction, map stitching, precise targeting, dead reckoning, and navigation. *Izv. South. Fed. Univ. Eng. Sci.* **2010**, *104*, 92–102, (In Russian, with English Abstract).
52. Hirschmuller, H. Stereo processing by semiglobal matching and mutual information. *IEEE Trans. Pattern Anal. Mach. Intell.* **2008**, *30*, 328–341. [CrossRef]
53. Watson, D. *Contouring: A Guide to the Analysis and Display of Spatial Data*; Pergamon Press: Oxford, UK, 1992; 321p.
54. Kurkov, V.M.; Kiseleva, A.S. DEM accuracy research based on unmanned aerial survey data. *ISPRS Int. Arch. Photogramm. Remote Sens. Spat. Inf. Sci.* **2020**, *XLIII-B3-2020*, 1347–1352. [CrossRef]
55. Shary, P.A.; Sharaya, L.S.; Mitusov, A.V. Fundamental quantitative methods of land surface analysis. *Geoderma* **2002**, *107*, 1–32. [CrossRef]
56. Florinsky, I.V. An illustrated introduction to general geomorphometry. *Prog. Phys. Geogr.* **2017**, *41*, 723–752. [CrossRef]
57. Florinsky, I.V.; Pankratov, A.N. A universal spectral analytical method for digital terrain modeling. *Int. J. Geogr. Inf. Sci.* **2016**, *30*, 2506–2528. [CrossRef]
58. Florinsky, I.V.; Kurkov, V.M.; Bliakharskii, D.P. Geomorphometry from unmanned aerial surveys. *Trans. GIS* **2017**, *22*, 58–81. [CrossRef]
59. Tveritinova, T.Y.; Beloborodov, D.E. Mud volcanoes in the neotectonic structure of the Taman Peninsula. *Dyn. Geol.* **2020**, *2*, 157–186. (In Russian)

60. Trikhunkov, Y.I. Neotectonic transformation of Cenozoic fold structures in the northwestern Caucasus. *Geotectonics* **2016**, *50*, 509–521. [CrossRef]
61. Engibarian, A.A. Lithological, Facies, and Tectonic Criteria for the Oil and Gas Content of the Meso-Cenozoic Deposits of the Taman Peninsula. Ph.D. Thesis, North-Caucasian State Technical University, Stavropol, Russia, 2006; 217p. (In Russian).
62. Lukina, N.V.; Karakhanyan, A.S.; Senin, B.V.; Skaryatin, V.D.; Trifonov, V.G. Linear and ring structures of the Crimean–Caucasian Region. In *Space Remote Sensing Data in Geology*; Trifonov, V.G., Makarov, V.I., Safonov, Y.G., Florensky, P.V., Eds.; Nauka: Moscow, Russia, 1983; pp. 195–206. (In Russian)
63. Tveritinova, T.Y.; Beloborodov, D.E.; Likhodeev, D.V. Mud volcanoes in the structure of the Kerch Peninsula. *Dyn. Geol.* **2020**, *1*, 38–54. (In Russian)
64. Beloborodov, D.E.; Tveritinova, T.Y. Structural position of mud volcanoes in the interpericlinal Kerch-Taman zone. In *Fundamental Problems of Tectonics and Geodynamics: Proc. LII Tectonic Meeting*; Degtyarev, K.E., Ed.; Geos: Moscow, Russia, 2020; Volume 1, pp. 65–69. (In Russian)
65. Hengl, T.; Reuter, H.I. (Eds.) *Geomorphometry: Concepts, Software, Applications*; Elsevier: Amsterdam, The Netherlands, 2009; 796p.
66. Wilson, J.P. *Environmental Applications of Digital Terrain Modeling*; Wiley: Hoboken, NJ, USA, 2018; 360p.
67. Luftwaffe and Allied Aerial Reconnaissance Archives. Research and Digitizing, 2013–2020. Available online: https://www.luftfoto.ru/index.html (accessed on 6 November 2020).